

WHEN VISIBLE-TO-THERMAL FACIAL GAN BEATS CONDITIONAL DIFFUSION

Catherine Ordun^{*,†} Edward Raff^{*,†} Sanjay Purushotham[†]

[†]University of Maryland, Baltimore County

^{*}Booz Allen Hamilton

ABSTRACT

Thermal facial imagery offers valuable insight into physiological states such as inflammation and stress by detecting emitted radiation in the infrared spectrum, which is unseen in the visible spectra. Telemedicine applications could benefit from thermal imagery, but conventional computers are reliant on RGB cameras and lack thermal sensors. As a result, we propose the Visible-to-Thermal Facial GAN (VTF-GAN) that is specifically designed to generate high-resolution thermal faces by learning both the spatial and frequency domains of facial regions, across spectra. We compare VTF-GAN against several popular GAN baselines and the first conditional Denoising Diffusion Probabilistic Model (DDPM) for VT face translation (VTF-Diff). Results show that VTF-GAN achieves high quality, crisp, and perceptually realistic thermal faces using a combined set of patch, temperature, perceptual, and Fourier Transform losses, compared to all baselines including diffusion.

Index Terms— GAN, Diffusion, Thermal, FER

1. INTRODUCTION

In thermal physiology, facial temperatures correlate to inflammation, emotional states, and cognitive stress [1]. In turn, telemedicine applications could use thermograms as a non-invasive way to assess patient health but typically cannot access expensive, specialized thermal cameras. As a result, we investigate the feasibility of using conditional Generative Adversarial Networks (cGAN) as a proxy for thermal sensors to generate thermal faces. The GAN framework has been applied successfully in both directions of Visible-to-Thermal (VT) and Thermal-to-Visible (TV) for person re-identification [2, 3, 4, 5, 6, 7, 8, 9, 10, 11, 12]. For facial VT translation, paired methods are preferable, in order to preserve the physiological mapping which is considered a biometric [13, 14, 15]. Yet, few works have explored how to estimate temperature from thermogram pixels where some works use metadata supplied by the camera, that demonstrate high quality results [16, 17]. More recently, works using diffusion models, formally known as Denoising Diffusion Probabilistic Models (DDPM) [18, 19], have enabled an alternate framework to generate diverse, high resolution art. A limited number of works have

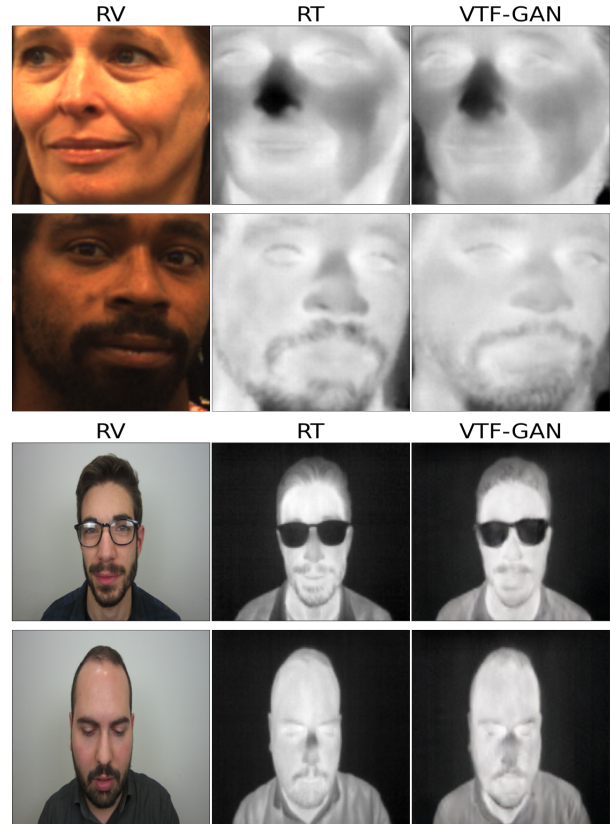


Fig. 1: Sample thermal faces generated by our proposed approach, the VTF-GAN, showing diverse faces at non-forward looking angles in addition to obfuscation such as glasses. RV=Real Visible, RT=Real Thermal.

explored TV diffusion [20]. While current works are promising, they still fail to yield crisp, high resolution thermal images due to the need to learn regional structures, temperature, coarse and fine frequencies simultaneously across spectra. To this aim, our contributions are:

- The Visible-to-Thermal Facial GAN (VTF-GAN) that learns thermal patch structure and temperature estimation.
- Two VTF-GAN variants designed to learn the frequency domain through a Fourier Transform Loss.

- Comparison against four GAN baselines and diffusion, through the first application of VT face translation using a conditional diffusion model (VTF-Diff).

2. RELATED WORKS

2.1. Thermal Physiology

Through the use of thermal sensors (e.g. cameras), thermal images visualize heat in the Long-Wave Infrared (LWIR) spectrum ($8\mu m - 15\mu m$). In thermal physiology, the facial temperatures correlate to inflammation, as well as emotional states such as empathy, distress, and cognitive stress [1, 21, 22, 23, 24]. Its mechanism is based on how the Autonomic Nervous System responds to psychological stimuli, by innervating blood vessels that line the surface of the face as shown in Figure 2 [22, 25, 26, 24].

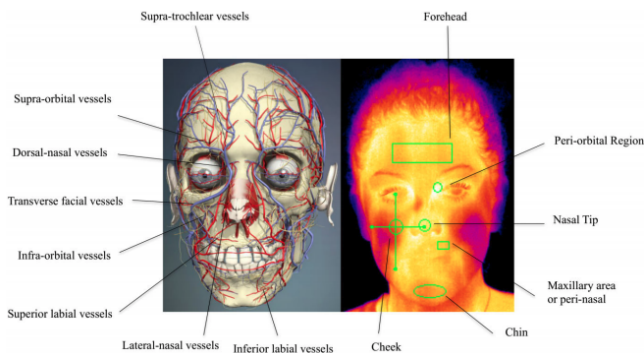


Fig. 2: Thermal Physiology. Emotional stimuli innervates blood vessels lining the surface of the face, which in turn release heat that is detected by thermal sensors. [1, 22]

2.2. Image-to-Image Translation

Since the introduction of the pix2pix [27] and CycleGAN [28] frameworks, GANs have been used as the defacto framework for translating one image modality to another. pix2pix uses conditional GANs (cGAN) where the generator is conditioned on an input sample, x , in order to generate an output image, y , thereby learning a deterministic mapping of $G(x, z) \rightarrow y$. Popular examples include *night* \leftrightarrow *day*, *horse* \leftrightarrow *zebra*, and novel house floor plan generation [29].

There are two approaches to image translation. The first is the paired approach, used by pix2pix, where x_i and y_i are pre-paired sets of images $(x_i, y_i)_{i=1}^N$ and y_i acts as a supervised label. The second approach uses unpaired datasets. There is a source dataset of images $x_{i=1}^N (x_i \in X)$ and target dataset $y_{i=1}^M (y_i \in Y)$. A substantial number of works largely follow the unpaired approach such as StarGAN [30], MUNIT [31], and FastCUT [32] to generate diverse artistic samples. These models have been benchmarked with images in the visible spectra, consisting of natural scenes, human sketches,

cartoons, art work, and illustrations. More recently, works using diffusion models [18, 19, 33, 34] that do not rely on the typical GAN setup, such as the Img2Img Stable Diffusion [35] application, allows for greater diversity in the generation of diverse, high resolution art. But, sampling remains slower than generating samples using GAN.

2.3. Visible-to-Thermal (VT) Image Translation

A small number of recent studies have emerged focusing on VT translation for cityscape and full body [16, 36, 37, 38] thermal generation. For specifically facial VT translation, paired translation methods are used in order to preserve the mapping between the visible and thermal physiology of the subject, which is considered a biometric [25]. Examples include the favtGAN approach [13] where thermal faces are generated by modifying a PatchGAN discriminator [27] to learn auxiliary thermal sensor classes from a combination of different datasets. Mallat et al. apply a Cascaded Refinement Network (CRN) [39] based on progressively upsampled feature maps [14, 40]. Pavez et al. generates a set of stylized thermal facial images using the GansNRoses [41] architecture for thermal facial recognition experiments [42], and [15] uses StyleGAN2 to generate random high resolution thermal faces that are not mapped to existing visible faces.

2.4. VT with Temperature Guidance

Few works have explored how to learn the explicit mapping between thermogram pixels and temperature. For example, with ThermalGAN [16], the authors pass a segmented thermal image into a modified U-NET [43] generator to output multiple thermal masks [28]. However, this vector was not learned, but rather provided as metadata. The metadata can be affixed with variables such as Planck constants and emissivity where temperature values are directly provided, or can be calculated using thermodynamic equations from software. For example, Cao et al., [17] minimize a temperature loss using a “temperature matrix” provided as metadata in the form of .bmp files from the Carl Database [44] through a pix2pix cGAN. Their temperature vector is composed of a single scalar value duplicated across the matrix representing only the forehead temperature, whereas ThermalGAN’s vector consists of undisclosed background and object temperatures. In our approach, we seek to approximate a temperature vector without relying on rare metadata, so that the model will learn temperature-to-pixel mappings through a temperature loss function.

3. PROPOSED METHOD

3.1. Architecture

We present three architectures of the VTF-GAN implementation: 1) VTF-GAN is our baseline model that composes four

losses for structural patch similarity, temperature vector approximation, perceptual similarity, in addition to the adversarial loss; 2) VTF-GAN-FFT-P adds a Fourier Transform loss [45] by calculating amplitude and phase of each patch; 3) VTF-GAN-FFT-G uses the same Fourier Transform loss but only calculates the amplitude and phase of the generated thermal face, not its patches.

3.2. VTF-GAN Baseline

The baseline VTF-GAN architecture shown in Figure 3. We add to the U-NET [43] generator (G), BlurPool layers [46] which anti-aliases the encoding and decoding modules and have been applied to medical tasks like ultrasound image segmentation [47]. We add BlurPool layers to the PatchGAN [27] Discriminator (D) in addition to spectral normalization [48] for training stability. G produces a fake thermal facial image, \hat{B} from an input visible facial image, A : $\hat{B} = G(A; \theta^G)$. Four losses are calculated during the VTF-GAN generator phase: (1) patch loss (L_{patch}), (2) temperature loss (L_{temp}), (3) perceptual similarity loss (L_{perc}), and a (4) relativistic adversarial loss (L_{GAN}). Since D is a PatchGAN discriminator, it accepts the pair ($A, G(A; \theta^G)$) or (A, B), and outputs probability values across 16 x 16 patches for fakeness (\hat{y}_f) and realness (\hat{y}_r). The D outputs a fake (L_{adv}^f) and real (L_{adv}^r) relativistic adversarial loss.

G consists of six encoder modules: Conv2D (4x4 kernel, stride=1, padding=1), LeakyReLU, and BlurPool (stride=2) layers. The five decoder modules consist of: Conv2D (4x4 kernel, stride=2, padding=1), BlurPool (stride=1), InstanceNorm2D, and ReLU layers. We apply dropout = 0.5 at encoder modules 3 and 4 and decoder modules 2 and 3. The D consists of four blocks: Conv2D (4x4 filter, stride=1, padding=1), LeakyReLU, and BlurPool (stride=2) layers, normalized using spectral normalization.

3.3. Patch Loss

The L_{patch} loss is used to learn structural similarity of generated thermal patch regions of the face, when compared to the real thermal image, B . It uses a triplet loss [49] shown in Equation 1. The distance between two samples is the L2 norm: $d(x, y) = \|x - y\|_2$, where we use margin = 1. \hat{B} and B is split into $K = 16$ which signifies 16 patches. After empirical investigations exploring 4 patches, we find that 16 patches leads to higher quality thermal images. For each patch k , the L_{patch} loss is calculated with the following inputs: $anchor = \hat{B}_k$, $positive = B_k$, and the negative (n) is a randomly selected patch drawn from any of the real thermal image patches, B_k^* . For each \hat{B} in the mini-batch, the patch loss is calculated in Equation 1.

$$L_{patch} = \frac{1}{K} \sum_{k=1}^K \max\{d(\hat{B}_k, B_k) - d(\hat{B}_k, B_k^*) + 1, 0\} \quad (1)$$

3.4. Temperature Loss

The L_{temp} is used to learn the mapping between facial temperatures and pixel values, approximating a temperature vector which has been applied in similar studies but is taken directly from camera metadata, never estimated. In Figure 4a, it shows the proprietary schematic of how Flir, Inc., a thermal camera manufacturer, conceptually maps temperature to different color grades in its palettes. We use a simple linear mapping to copy this idea.

For the real thermal B and fake thermal \hat{B} , we use raw pixel values from 0 to 255, then linearly map them to a single temperature value between 24.0 to 38.0 Celsius (temperature of human faces). The temperature loss (L_{temp}) shown in Equation 2 is a triplet loss where B is perturbed with jitter (brightness=0.5, contrast=0.75, saturation=1.5, hue=0.5) to create a negative sample. As shown in Figure 1, \hat{B} first outputs a single channel fake temperature vector using the red channel, \hat{B}_T , which is used as the anchor. The real thermal image B outputs B_T as the positive input, and the negative comes from the jittered B which outputs the temperature vector, B_{Tj} .

$$L_{temp} = \max\{d(\hat{B}_T, B_T) - d(\hat{B}_T, B_{Tj}) + 1, 0\} \quad (2)$$

3.5. Perceptual Loss

The third loss, L_{perc} , is a common perceptual similarity loss between B and \hat{B} , using LPIPS [51, 52, 53]. Per Equation 3, ϕ is the feature extractor using the VGG-16 network [54], τ transforms network embeddings to the LPIPS score, which is calculated and averaged over n layers.

$$L_{perc} = \sum_n \tau^n(\phi^n(\hat{B}) - \phi^n(B)) \quad (3)$$

3.6. Adversarial Loss

The fourth loss is a relativistic adversarial L_{GAN} loss used to predict the fake or realness of the generated thermal face. The goal of relativistic loss is to increase the probability that B is more realistic than \hat{B} [55], thereby focusing on the relative realness as opposed to its absolute value [56]. As such, L_{GAN} calculates the distance between the fake \hat{y}_f and real \hat{y}_r probabilities, against the ground-truth valid (V) labels. In the generator phase, G passes both (A, B) and ($A, G(A; \theta^G)$) to the discriminator, which outputs probabilities \hat{y}_r or \hat{y}_f . The relativistic loss accepts as input, the distance between both probabilities (δ^{G^F}) per Equations 4 and 5. Per Equation 6, the L_{GAN} is a binary cross entropy (BCE) with logits loss ($V = 0.9$, averaged over the mini-batch, N). The total G loss is shown in Equation 7.

$$\hat{y}_r = D(A, B; \theta^D); \quad \hat{y}_f = D(A, G(A; \theta^G)); \theta^D \quad (4)$$

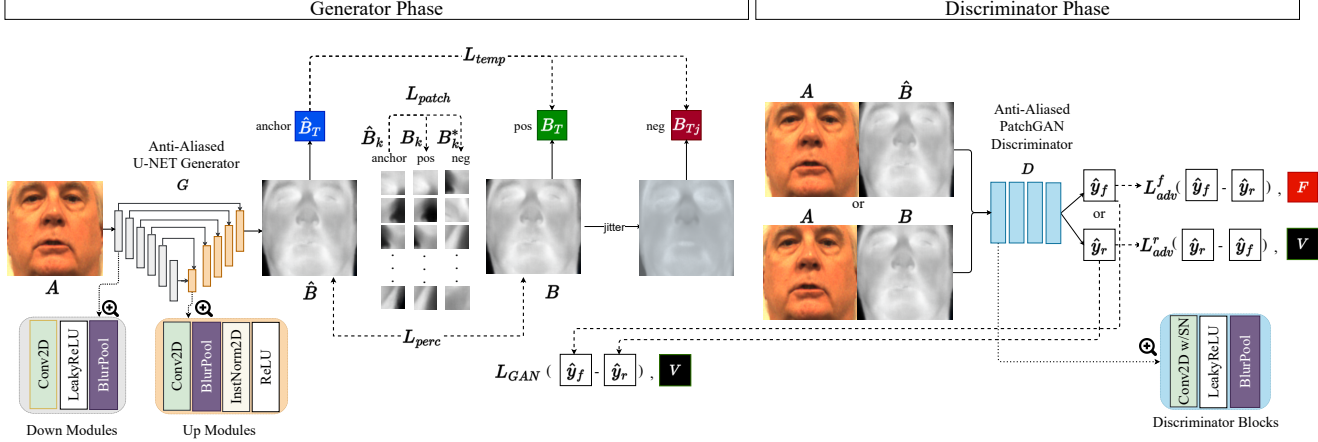


Fig. 3: Overview of VTF-GAN. In the Generator Phase, the Anti-Aliased U-NET Generator (G) takes visible image, A , and outputs generated thermal face, \hat{B} . The \hat{B} is forwarded to the Anti-Aliased PatchGAN Discriminator (D) that also contains BlurPool layers, which outputs a tensor with fake or real (\hat{y}_f, \hat{y}_r) probability values per patch. These are used to calculate the relativistic adversarial loss against V, F (valid and fake labels).

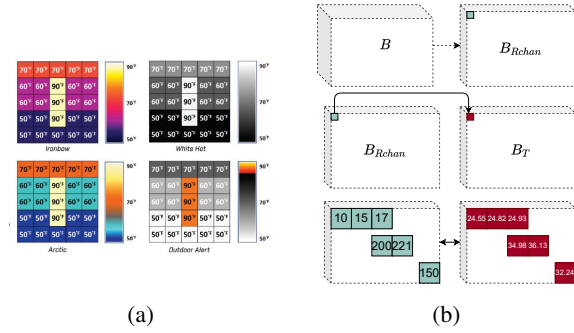


Fig. 4: Temperature Guides. (a) Notional temperature palettes provided from FLIR, Inc. [50]. (b) Proposed method to map raw pixel values with temperatures for both real B and fake \hat{B} thermal images.

$$\delta^{G^F} = \hat{y}_f - \hat{y}_r \quad (5)$$

$$L_{bce}^{GAN}(\delta^{G^F}, V) = -\frac{1}{N} \sum_{i=1}^N [V_i \log \sigma(\delta_i^{G^F}) + (1 - V_i) \log(1 - \sigma(\delta_i^{G^F}))] \quad (6)$$

$$L_G = L_{bce}^{GAN} + L_{perc} + L_{temp} + L_{patch} \quad (7)$$

3.7. Discriminator Loss

Similar to L_{GAN} , the adversarial relativistic loss computes the distance between the \hat{y}_r or \hat{y}_f , relative to each other as shown in Equation 9.

$$\hat{y}_r = D(A, B; \theta^D); \quad \hat{y}_f = D(A, G(A); \theta^D) \quad (8)$$

$$\delta^R = \hat{y}_r - \hat{y}_f; \quad \delta^F = \hat{y}_f - \hat{y}_r \quad (9)$$

These are used to calculate the real and fake adversarial losses shown in Equations 10 and 11, which are averaged to output the total discriminator loss, L_D in Equation 12 (where $V = 0.9, F = 0.0$). The relativistic loss is also binary cross entropy loss with logits. The total training objective is as follows in Equation 13.

$$L_{adv}^r = L_{bce}^R(\delta^R, V) = -\frac{1}{N} \sum_{i=1}^N [V_i \log \sigma(\delta_i^R) + (1 - V_i) \log(1 - \sigma(\delta_i^R))] \quad (10)$$

$$L_{adv}^f = L_{bce}^F(\delta^F, F) = -\frac{1}{N} \sum_{i=1}^N [F_i \log \sigma(\delta_i^F) + (1 - F_i) \log(1 - \sigma(\delta_i^F))] \quad (11)$$

$$L_D = \frac{1}{2} [L_{adv}^r + L_{adv}^f] \quad (12)$$

$$G^* = \arg \min_G \max_D L_G + L_D \quad (13)$$

3.8. Fourier Transform Loss

Visible and thermal images differ in frequency and resolution, since each have been captured in completely different optical spectra. For example, Figure 5 shows the 2D Discrete Fourier Transform (DFT) from ground truth samples of our datasets. As a result, we propose adding a Fourier Transform loss that was introduced for super-resolution on GANs [45], and apply it towards the VT facial translation problem for the VTF-GAN-FFT-P and VTF-GAN-FFT-G variants. The motivation is to not only map the visible-to-thermal pixel space, but also

achieve similarity between high and low frequencies such as hair, teeth, and glasses.

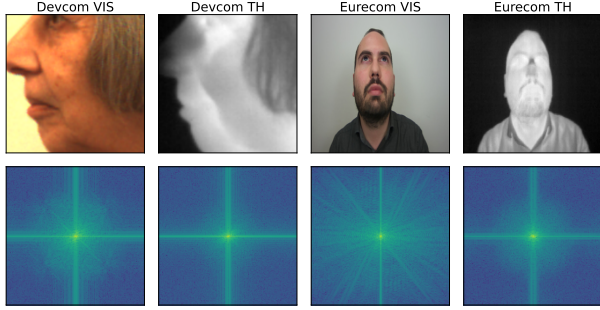


Fig. 5: Examples of Discrete Fourier Transforms on ground truth samples of the Devcom (left) and Eurecom (right) dataset. VISIBLE and THERMAL. Notice that both modalities have different spectral densities.

For a given image, $x \in \mathcal{R}^{H \times W \times C}$, the DFT decomposes it from the spatial to Fourier domain, $\mathcal{F}\{x\}_{u,v}$. It represents a complex array that consists of real (\mathcal{R}) numbers and imaginary (\mathcal{I}) numbers, where u, v are frequency components. Due to Hermitian symmetry in the Fourier domain for real values, redundant complex components can be removed so that only half the values remain but retains the same information.

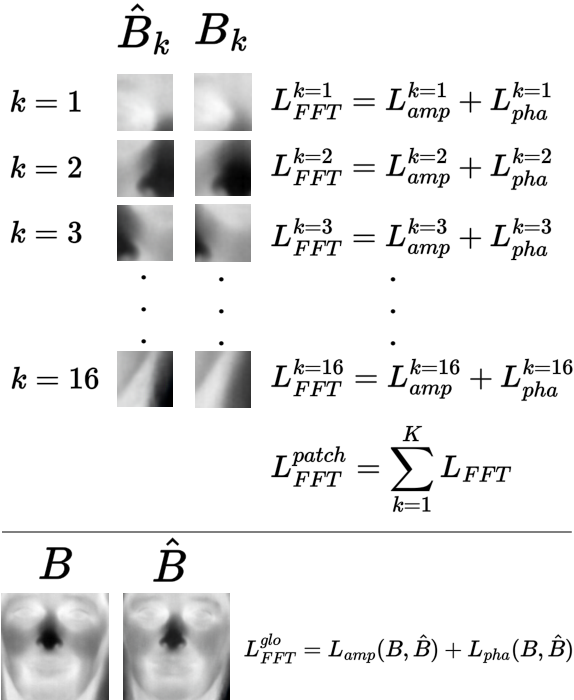


Fig. 6: Diagram of FFT patch method. Illustrates calculating the Patch Loss by patches, or by the entire global facial image.

We illustrate our approach in Figure 6. For the VTF-GAN-FFT-P model, the amplitude in Equation 14 and phase

in Equation 15 are calculated for each real (B_k) and fake (\hat{B}_k) thermal patch $k \in K$ where $K = 16$, so that $x = B_k \vee \hat{B}_k$.

$$|\mathcal{F}\{x\}_{u,v}| = |X_{u,v}| = \sqrt{\mathcal{R}\{X_{u,v}\}^2 + \mathcal{I}\{X_{u,v}\}^2} \quad (14)$$

$$\angle \mathcal{F}\{x\}_{u,v} = \angle X_{u,v} = \text{atan2}(\mathcal{I}\{X_{u,v}\}, \mathcal{R}\{X_{u,v}\}) \quad (15)$$

$$L_{amp}^{patch} = \frac{1}{K} \sum_{k=1}^K \|(|\mathcal{F}\{B_k\}_{u,v}|) - (|\mathcal{F}\{\hat{B}_k\}_{u,v}|)\|_1 \quad (16)$$

$$L_{pha}^{patch} = \frac{1}{K} \sum_{k=1}^K \|(\angle \mathcal{F}\{B_k\}_{u,v}) - (\angle \mathcal{F}\{\hat{B}_k\}_{u,v})\|_1 \quad (17)$$

$$L_{FFT}^{patch} = 0.5 * (L_{amp}^{patch} + L_{pha}^{patch}) \quad (18)$$

For the VTF-GAN-FFT-G model, the amplitude and phase are only calculated for the generated thermal face, not the patches. Therefore, it uses the real and fake global thermal images (B and \hat{B} , respectively) so that $x = B \vee \hat{B}$. For the patch and global forms, the L1 loss is used to calculate an amplitude and phase loss in Equations 16, 17, 19, and 20. The FFT loss for the VTF-GAN-FFT-P is Equation 18, and for VTF-GAN-FFT-G it is Equation 21. The updated generator loss is shown in Equation 22. There is no change to the discriminator losses.

$$L_{amp}^{glo} = \|(|\mathcal{F}\{B\}_{u,v}|) - (|\mathcal{F}\{\hat{B}\}_{u,v}|)\|_1 \quad (19)$$

$$L_{pha}^{glo} = \|(\angle \mathcal{F}\{B\}_{u,v}) - (\angle \mathcal{F}\{\hat{B}\}_{u,v})\|_1 \quad (20)$$

$$L_{FFT}^{glo} = 0.5 * (L_{amp}^{patch} + L_{pha}^{patch}) \quad (21)$$

$$L_G = L_{bce}^{GAN} + L_{perc} + L_{temp} + L_{patch} + L_{FFT} \quad (22)$$

3.9. VTF-Diff

Recently, TV facial translation was explored using DDPM [20]. For a complete exposition of DDPM, we refer the reader to [18, 19, 33]. We offer the first VT facial translation DDPM called ‘‘VTF-Diff’’ shown in Figure 7, following the general conditional approach by [33]. Given a paired dataset $D = \{x_i, y_i\}_{i=1}^N$ where $x = a \in A$ and $y = b \in B$, the conditional distribution $p(y|x)$ can map many target, thermal images (y) to a single visible source, x . The VTF-Diff follows a forward Markovian diffusion process denoted by $q(y_t|y_{t-1})$, that gradually adds Gaussian noise to a high-resolution thermal image $y_0 \sim p(y|x)$ over T iterations. The forward process is denoted in the dashed blue line in Figure 7.

The process is reversed to recover the signal from the noise through a reverse Markov chain, conditioned on visible image, x . Shown in Figure 7 with the solid red line, it begins with a pure noise image $y_T \sim N(0, I)$. This noisy image is gradually refined through a series of timesteps according to the learned conditional distributions $p_\theta(y_{t-1}|y_t, x)$. The

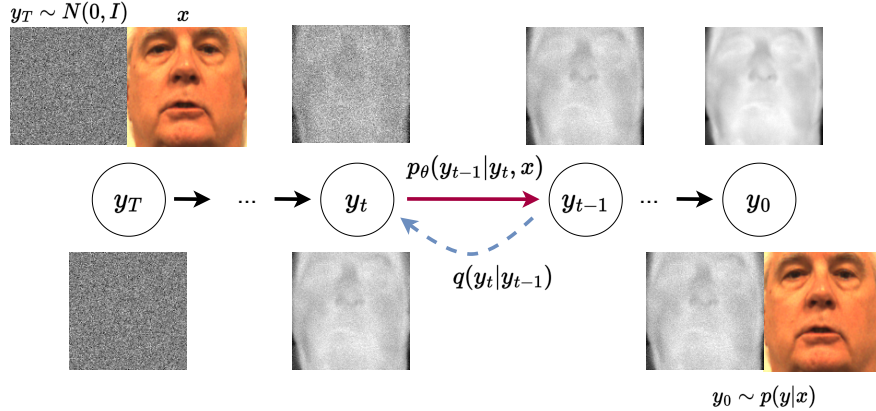


Fig. 7: Overview of VTF-Diff. The VTF-Diff forward process (q) (dotted blue line) gradually adds Gaussian noise to the thermal target conditioned on the visible input $y_0 \sim p(y|x)$. The reverse process (solid red line), p , iteratively denoises a pure noisy image to generate the thermal image, y_0 .

denoising model, f_θ is a U-NET with attention and residual blocks that takes as input, the source x , the noisy target image y_T , and predicts noise.

To implement, we train a 2D Conditional U-NET as the denoising model from the Hugging Face library, conditioning the input with the real visible image, and use a Mean Squared Error (MSE) loss to predict noise. We apply squared cosine for the noise scheduler [19], train for 500 timesteps, 200 epochs, a batch size of 12, using parallel GPUs, average mixed precision (AMP), and apply gray-scaling to both the visible and thermal images. Images generated are 128 x 128, due to limited compute. We find that applying grayscale transforms not only improves quality of the thermal image generated, but also reduces sampling times from approximately 30 sec./test image to 11.05 sec. on a single RTX 8000.

Table 1: Summary of Datasets used in Experiments

Dataset	# Subjects	# Train Pairs	# Test Pairs
Eurecom [57]	50	945	105
Original Devcom [58]	233	131,583	5590
5% Devcom	190	6580	280
Eur + 5% Devcom (ED)	240	7,525	385

4. EXPERIMENTS

4.1. Datasets

We use two paired VT facial datasets which are the Eurecom [57] and the Devcom ARL Polarimetric Thermal Face [59] datasets shown in Table 1. Both datasets were captured with Uncooled VOx microbolometer thermal sensors, and consist of multiple poses and forward looking angles in addition to different lighting conditions. The Eurecom dataset provided

individual thermal and visible images of exact scale for alignment, while the Devcom dataset provided metadata coordinates to crop and align images. The Devcom dataset offers a more close-up view of the subjects whereas the Eurecom faces are set farther back and zoomed out. Examples are shown in Figure 5. Additionally, the Devcom dataset is also more ethnically diverse than Eurecom. For example, based on a manual, subjective, labeling effort, approximately 25% of subjects are non-white, compared to less than 10% in the Eurecom dataset. Further, we take a 5% random sample of the Devcom dataset and train our models and comparison baselines on 6,580 training pairs. We do this in order to mimic the limited nature of cross-spectral medical datasets like CT scans and X-rays which often number in less than a few thousand training pairs [60, 61, 62]. However, we also present results on the best model using the entire Devcom dataset.

4.2. Setup

We conduct experiments on four baselines: 1) pix2pix [27], 2) CycleGAN [28], 3) ThermalGAN [16], and 4) favtGAN [13]). These baselines were selected based on their use in existing VT/TV studies such as [7, 17, 36, 42]. We combine the Eurecom and Devcom datasets together in order to train the favtgan [13] model that requires two datasets captured from similar thermal sensors. We compare the baselines against VTF-GAN and its variants VTF-GAN-FFT-P and VTF-GAN-FFT-G. Further, we trained pix2pixHD [63], FastCUT [32], GansNRoses [41], StarGAN [30], and MUNIT [31], but excluded the results due to distortion and failure to translate into the thermal modality, where results are shown in Figure 10.

4.3. Evaluation

We measure quality of generated Eurecom and Devcom thermal faces using the Frchet Inception Distance (FID) [64]

Table 2: Quantitative Results for Quality of Eurecom and Devcom Generated Thermal Faces. Scores in **bold** are best results. Next to each metric, we provide the relative percentage change based on the best performing model in **bold**. * Devcom Full Dataset, percentage change in respective directions compared to best performing scores for Devcom experiment.

Eurecom						
Baselines	FID↓	(%)	DBCNN↑	(%)	MSE SPEC↓	(%)
pix2pix[27]	115.932	-39.4%	22.272	26.1%	0.851	0.0%
CycleGAN[28]	146.440	-52.0%	25.955	8.2%	1.181	-28.0%
ThermalGAN[16]	328.046	-78.6%	20.014	40.3%	2.317	-63.3%
favtGAN[13]	337.990	-79.2%	25.841	8.6%	1.241	-31.5%
VTF-Diff	80.212	-12.5%	28.076	0.0%	1.072	-20.7%
Ours	FID↓	(%)	DBCNN↑	(%)	MSE SPEC↓	(%)
VTF-GAN	70.221	0.0%	27.738	1.2%	1.036	-17.9%
+FFT-P	75.935	-7.5%	25.539	9.9%	1.007	-15.5%
+FFT-G	74.814	-6.1%	26.111	7.5%	1.103	-22.9%
Devcom						
Baselines	FID↓	(%)	DBCNN↑	(%)	MSE SPEC↓	(%)
pix2pix[27]	101.305	-53.3%	33.295	4.0%	0.896	-3.3%
CycleGAN[28]	67.063	-29.4%	29.122	18.9%	0.920	-5.8%
ThermalGAN[16]	347.091	-86.4%	32.934	5.1%	1.984	-56.4%
favtGAN[13]	244.812	-80.7%	32.287	7.2%	2.030	-57.3%
VTF-Diff	93.320	-49.3%	28.810	20.2%	1.646	-47.4%
Ours	FID↓	(%)	DBCNN↑	(%)	MSE SPEC↓	(%)
VTF-GAN	51.874	-8.7%	33.605	3.0%	0.866	0.0%
+FFT-P	48.737	-2.8%	34.622	0.0%	0.873	-0.8%
+FFT-G	47.351	0.0%	34.338	0.8%	0.876	-1.1%
Devcom - Full Dataset						
Ours	FID↓	(%)	DBCNN↑	(%)	MSE SPEC↓	(%)
+FFT-G	21.303	55.01%*	33.901	2.07%*	0.834	3.69%*

score, the Deep Bilinear CNN (DBCNN) [65], and MSE between the generated and real thermal image magnitude spectra. DBCNN measures distortion in GAN generated images and is modeled on the concept of two-factor variation in bilinear CNNs used to simultaneously assess synthetic and authentic distortions. Measuring error of magnitude spectra provide intuition about the similarity of the generated images’ low and high frequencies. We do not report the Structural Similarity Index Measure (SSIM) [66] as a metric for perceptual quality. Besides, studies have examined how SSIM can behave contradictory to human perception leading to misleading results since they are sensitive to small changes in color gradients, blur, and minor misalignments, especially for synthetic samples [67, 68, 69, 70].

4.4. Implementation Details

We train models using three NVIDIA Quadro RTX 8000s and two NVIDIA RTX A6000s. All models were trained using the PyTorch library. Settings for all baselines include batch size 32, 200 epochs, using average mixed precision (AMP), and gradient scaling, where the VTF-GAN and its variants use a learning rate of 0.0002, and Adam Optimizer ($\beta_1 = 0.50$, $\beta_2 = 0.99$).

5. RESULTS

5.1. Quantitative Results

Quantitative results are shown in Table 2. The table shows each metric along with its respective, relative percentage change when compared to the best scoring model. Against all baselines for both Eurecom and Devcom, the VTF-GAN and its variants show the best FID scores. For Eurecom, VTF-GAN and all its variants outperform the FID score, specifically demonstrating a 12.5% decrease when VTF-GAN is compared to VTF-Diff. VTF-Diff only slightly outperforms VTF-GAN for DBCNN at a 1.2% increase. The pix2pix model shows the best MSE SPEC (spectrograms) at 17.9% decrease compared to VTF-GAN.

For the closer-up faces of the Devcom dataset, the VTF-GAN and its variants outperform all baselines. For FID, the VTF-GAN-FFT-G demonstrates a significant 49.3% decrease in FID compared to VTF-Diff, with the next best baseline as CycleGAN (-29.4%). For DBCNN, the VTF-GAN-FFT-P outperforms against the VTF-Diff at a 20.2% increase. VTF-GAN beats VTF-Diff for MSE SPEC scores with a relative decrease of 47.4%.

We extended the experiments and trained on the entire De-

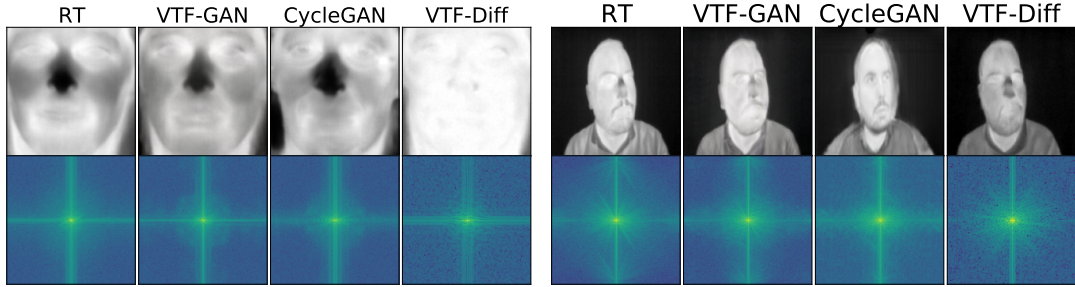


Fig. 8: Magnitude Spectra Samples for Devcom and Eurecom Generated Thermal Faces, comparing VTF-GAN, Best Baseline, and VTF-Diff.

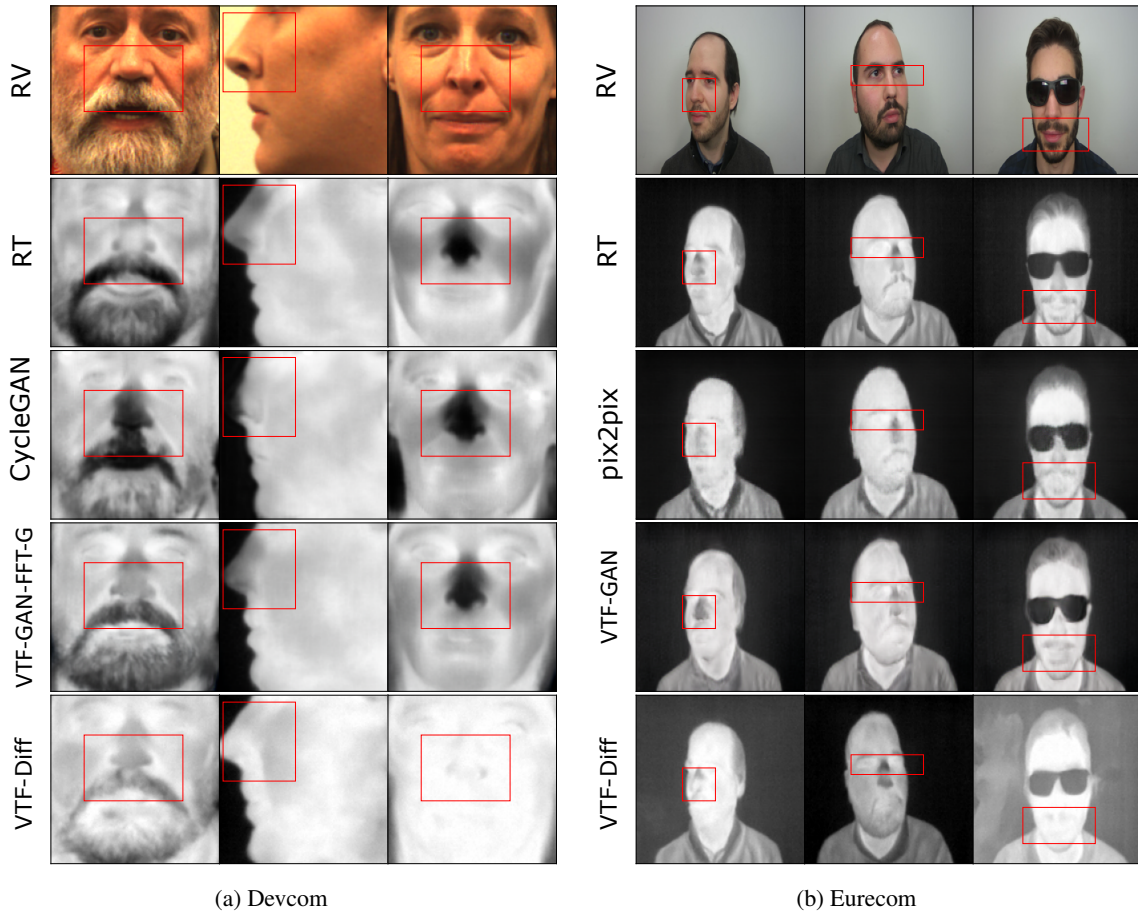


Fig. 9: Close-up Generated Thermal Faces Comparing VTF-GAN to Next Best Model. The red regions indicate areas of physiological interest. Notice the sharpness and clarity of our samples (Row 4 of each subset), when compared to the next best model based on FID score. The temperature distribution of dark (cold) and light (warm) pixels is maintained on the nose and mouth regions, while also showing details and articulation of eyes, and maintaining evenness while limiting blur and distortion.

vcom dataset using the best VTF-GAN variant, VTF-GAN-FFT-G. Doing so led to a significant decrease in FID and MSE SPEC scores. In Table 2, we show that training on the entire dataset led to a 55.01% decrease in FID compared to the VTF-GAN-FFT-G (47.351) when trained on the limited Devcom dataset. Similarly, the MSE SPEC scores decrease by 3.69%

compared to the VTF-GAN (0.866) baseline. However, the DBCNN scores do not improve, leading to a 2.07% increase of score when compared to the VTF-GAN-FFT-P DBCNN score (34.622).

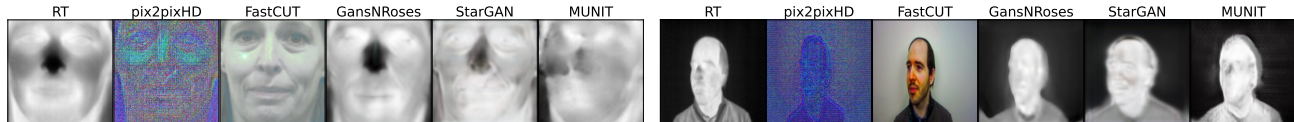


Fig. 10: Failed GAN baselines. Samples from additional GAN baselines which led to distorted results: pix2pixHD, FastCUT, GansNRoses, StarGAN, and MUNIT.

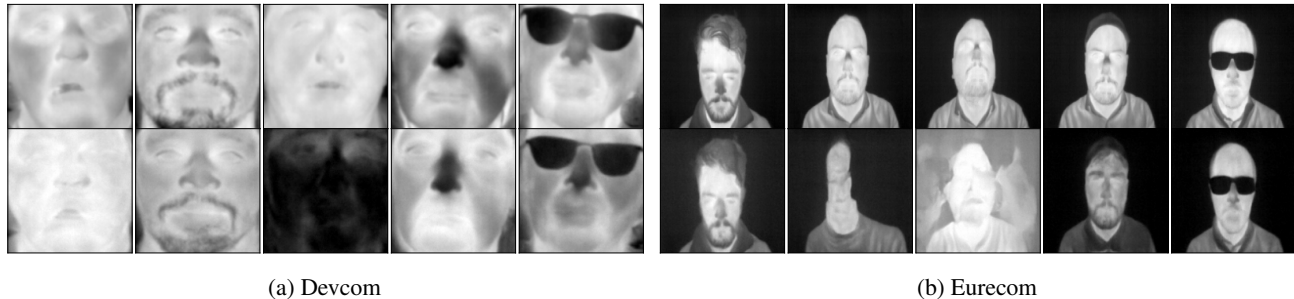


Fig. 11: Additional VTF-Diff Samples. For each figure, Top: Real Thermal, Bottom: Generated Thermal

5.2. Qualitative Results

In Figure 8, we provide samples that compare the generated thermal faces from our approach, the best baseline, and VTF-Diff. In addition, we show their respective magnitude spectra to demonstrate the variation in spectral density where the VTF-GAN spectrogram is closer to the real thermal spectrogram. The VTF-GAN models translate high frequency edges such as hair, eyes, glasses, and teeth, with higher resolution and crispness, when compared to pix2pix, CycleGAN, and favtGAN. Unfortunately, the ThermalGAN model failed to translate appropriately. Here we show that ThermalGAN is not a feasible model for facial translation. We believe that ThermalGAN is best suited for cityscapes and whole body views, where it can apply latent codes learned from segmentation maps of discretely bound objects. The magnitude spectra show an alternative visualization of how to assess image quality. For example, blurred or distorted thermal faces lead to artifacts and checkerboard patterns in the magnitude spectra.

In Figure 9, we show samples compared to the next best comparison model based on FID score which is CycleGAN for Devcom and pix2pix for Eurecom. The red boxes indicate areas of physiological interest [1, 71, 23]. For Devcom in Figure 9a, CycleGAN images distort the nose area by darkening and adding distortion, giving the illusion of extreme heat, or failing to generate the tip of the nose. CycleGAN appears to take visible features and colorize them in order to match a thermal style, as indicative of the eyes for the first and third subjects. The VTF-GAN Eurecom samples in Figure 9b are higher resolution than the pix2pix samples, translating details such as eyes with greater crispness while also preserving the temperature distributions of the nose regions. The VTF-Diff

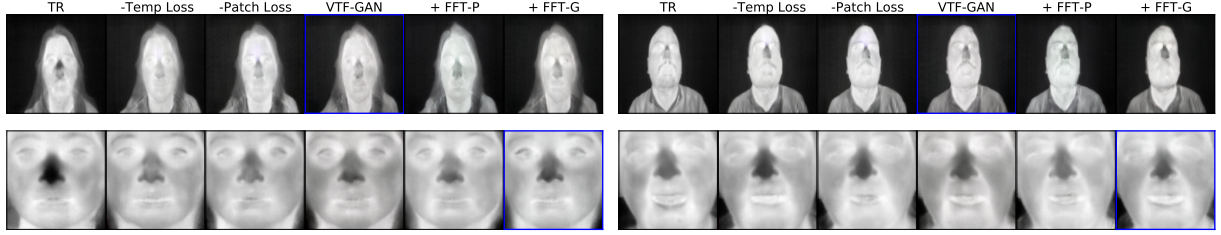
generates the geometry and subject identify with fair clarity but fails to generate the correct distribution of temperature.

5.3. Failures

We also show the failed results of other GAN baselines shown in Figure 10 for pix2pixHD [63], Fast CUT (Contrastive Unpaired Translation) [32], GansNRoses [41], StarGAN [30], and MUNIT [72]. We speculate the reason for these failed cases is the loss of the paired mapping between the visible and thermal faces since they represent an exact human physiological state in a single moment in time. Both the subject identity and their unique biometric temperatures need to be preserved for medical interpretation. When the mapping is decoupled in the pursuit of image or multimodal diversity, as these models are designed for, the translated results are poor. Unlike the failed GAN baselines, the VTF-Diff model shows some fair results in Figure 11, such as reconstructing identity in addition to nose temperature, geometric eye shapes, glasses, and facial hair. But most samples fail to generate the correct pixel-to-temperature distribution causing images to be too dark or too light. The majority of samples are inconsistent showing artifacts and distortion, despite the emergence of a few fair outputs.

6. ABLATION STUDY

The VTF-GAN-FFT-P and VTF-GAN-FFT-G architectures already ablate to the baseline VTF-GAN architecture, since it merely removes the Fourier Loss ($L_{FFT}^{patch} \vee L_{FFT}^{glo}$). Therefore, we remove the Patch Loss (L_{patch}) and the Temperature Loss (L_{temp}) from the VTF-GAN baseline, while holding all other losses fixed. As a reference, we compare the ablation



(a) Top: Eurecom Subject 1, Bottom: Devcom Subject 1

(b) Top: Eurecom Subject 2, Bottom: Devcom Subject 2

Fig. 12: Ablation Sample Results. When removing the Temperature and Patch Losses from the baseline VTF-GAN model, notice the loss of temperature distribution where the nose either becomes darker (colder) or lighter (warmer), compared to the real thermal (TR). For Eurecom, the VTF-GAN preserves the articulation, detail, and temperature evenness of the thermal image. For Devcom, the VTF-GAN-FFT-G best preserves the temperature of the nose and cheeks, while maintaining detail of the eyes. Blue borders indicate best performing model by FID score, across all experiments. TR: Real Thermal.

Table 3: Ablation Study Results for Eurecom and Devcom.

Eurecom			
Model	FID↓	DBCNN↑	MSE SPEC↓
VTF-GAN (-Temp Loss)	70.687	27.098	1.028
VTF-GAN (-Patch Loss)	71.140	26.694	1.068
VTF-GAN	70.221	27.738	1.036
VTF-GAN-FFT-P	75.935	25.539	1.007
VTF-GAN-FFT-G	74.814	26.111	1.103
Devcom			
Model	FID↓	DBCNN↑	MSE SPEC↓
VTF-GAN (-Temp Loss)	49.911	34.069	0.873
VTF-GAN (-Patch Loss)	47.437	33.853	0.875
VTF-GAN	51.874	33.605	0.866
VTF-GAN-FFT-P	48.737	34.622	0.873
VTF-GAN-FFT-G	47.351	34.338	0.876

results against the Eurecom best performing model which is the VTF-GAN (70.221). When removing the patch loss, all three scores (FID, DBCNN, and MSE SPEC) are negatively affected. By removing the Patch Loss then the Temperature Loss, the FID score increases from 70.221 to 70.687. Further, we use the best performing Devcom VTF-GAN-FFT-G model, as a reference. When removing the Patch and Temperature Loss from the VTF-GAN (which does not include a Fourier Loss), all three scores are negatively affected.

Samples are shown in Figure 12, where the blue border indicates the best performing VTF-GAN variant. The Devcom subjects retain geometric fidelity over the ablations, however removal of Patch and Temperature Losses lead to either warmer (Figure 12a) or colder (Figure 12b) pixels, inconsistent from the ground truth (“TR”). Similarly, the Eurecom subjects lose temperature fidelity and exhibit blurriness as the Patch Loss is ablated followed by the Temperature Loss.

7. LIMITATIONS

The current study explores feasibility of generating thermal faces for telemedicine applications, but has not been tested in dynamic environments across multiple extraneous environmental and physiological conditions. Multiple exogenous factors not represented in the experimental datasets such as changes in body temperature, demographics, weather conditions, and exercise as explained in [26], can influence facial temperature and as a result, the visualized thermogram.

Next, greater investigation is required to understand the ethical impacts of generating thermal faces, especially with regards to privacy of underrepresented minorities. Given the lack of minority faces in TV datasets, the ability to generate ethnic features such as eyes and hair is often overwhelmed by Caucasian features. However, the pursuit of increasingly accurate minority thermal face generation should be assessed for its motivation especially with regards to exploitation and privacy since anonymity from thermal images is not guaranteed [73].

8. CONCLUSION

We present the Visible-to-Thermal Facial GAN (VTF-GAN) that learns spatial and Fourier domain losses to generate detailed, high quality thermal faces from visible images. To evaluate our approach, we offer three architectures: 1) VTF-GAN, 2) VTF-GAN-FFT-P, and 3) VTF-GAN-FFT-G, where the latter two use a Fourier Transform Loss either across patches (P) or the entire global face (G). We compare our results against the pix2pix, CycleGAN, ThermalGAN, and favtgan baselines that use conditional GAN for image-to-image translation and train on two different, diverse VT paired facial datasets. Due to the popular emergence of diffusion models (DDPM), we also examine our results against a conditional DDPM implementation. As a result, we offer the first VT facial translation DDPM application as a baseline comparison called “VTF-Diff”.

Our results show that when measuring FID score, the VTF-GAN and its variants achieve significantly lower scores for generating thermal faces at different angles, demographics, and resolutions, when compared to the GAN baselines and VTF-Diff. Our FID scores demonstrate -12.5% for the Eurecom dataset and -49.3% for the Devcom dataset, when compared to VTF-Diff. Even though training on only 5% of the Devcom dataset leads to a significant improvement in FID, DBCNN, and MSE SPEC scores, training on the entire Devcom dataset leads to substantial scores that beat all baselines and the VTF-Diff.

9. REFERENCES

- [1] Stephanos Ioannou et al., “Thermal infrared imaging in psychophysiology: potentialities and limits,” *Psychophysiology*, vol. 51, no. 10, pp. 951–963, 2014.
- [2] Kancharagunta Kishan Babu et al., “PCSGAN: Perceptual cyclic-synthesized generative adversarial networks for thermal and nir to visible image transformation,” *arXiv*, 2020.
- [3] Cunjian Chen and Arun Ross, “Matching thermal to visible face images using a semantic-guided generative adversarial network,” in *FG*, 2019.
- [4] Wei-Ta Chu et al., “A parametric study of deep perceptual model on visible to thermal face recognition,” in *VCIP*, 2018.
- [5] Naser Damer, Fadi Boutros, Khawla Mallat, Florian Kirchbuchner, Jean-Luc Dugelay, and Arjan Kuijper, “Cascaded generation of high-quality color visible face images from thermal captures,” *arXiv*, 2019.
- [6] Kenneth Lai and Svetlana N Yanushkevich, “Multi-metric evaluation of thermal-to-visual face recognition,” in *EST*, 2019.
- [7] Yawen Lu et al., “Bridging the invisible and visible world: Translation between rgb and ir images through contour cycle gan,” in *AVSS*, 2021.
- [8] Khawla Mallat et al., “Cross-spectrum thermal to visible face recognition based on cascaded image synthesis,” in *ICB*, 2019.
- [9] Mehmet Akif Özkanoğlu et al., “Infragan: A gan architecture to transfer visible images to infrared domain,” *Pattern Recognition Letters*, 2022.
- [10] Zhongling Wang et al., “Thermal to visible facial image translation using generative adversarial networks,” *IEEE Signal Processing Letters*, 2018.
- [11] He Zhang et al., “Synthesis of high-quality visible faces from polarimetric thermal faces using generative adversarial networks,” *IJCV*, 2019.
- [12] Teng Zhang et al., “TV-gan: Generative adversarial network based thermal to visible face recognition,” in *ICB*, 2018.
- [13] Catherine Ordun et al., “Generating thermal human faces for physiological assessment using thermal sensor auxiliary labels,” *ICIP*, 2021.
- [14] Khawla Mallat et al., “Facial landmark detection on thermal data via fully annotated visible-to-thermal data synthesis,” .
- [15] Gabriel Hermosilla et al., “Thermal face generation using stylegan,” *IEEE Access*, 2021.
- [16] Vladimir V Kniaz et al., “ThermalGAN: Multi-modal color-to-thermal image translation for person re-identification in multispectral dataset,” in *ECCV*, 2018.
- [17] Xingdong Cao et al., “Cross-spectrum thermal face pattern generator,” *IEEE Access*, 2022.
- [18] Jonathan Ho et al., “Denoising diffusion probabilistic models,” *Advances in Neural Information Processing Systems*, vol. 33, pp. 6840–6851, 2020.
- [19] Alexander Quinn Nichol et al., “Improved denoising diffusion probabilistic models,” in *ICML*. PMLR, 2021, pp. 8162–8171.
- [20] Nithin Gopalakrishnan Nair et al., “T2v-ddpm: Thermal to visible face translation using denoising diffusion probabilistic models,” *arXiv preprint arXiv:2209.08814*, 2022.
- [21] Mehdi Mirza and Simon Osindero, “Conditional generative adversarial nets,” *arXiv*, 2014.
- [22] Ioannis Pavlidis et al., “The imaging issue in an automatic face/disguise detection system,” in *IEEE Computer Vision Beyond the Visible Spectrum*, 2000.
- [23] Arcangelo Merla, “Revealing psychophysiology and emotions through thermal infrared imaging,” in *PhyCS*, 2014.
- [24] Ioannis Pavlidis et al., “Interacting with human physiology,” *Computer Vision and Image Understanding*, 2007.
- [25] Pradeep Buddharaju et al., “Physiology-based face recognition in the thermal infrared spectrum,” *IEEE TPAMI*, 2007.
- [26] Catherine Ordun et al., “The use of AI for thermal emotion recognition: A review of problems and limitations in standard design and data,” *AAAI*, 2020.

- [27] Phillip Isola et al., “Image-to-image translation with conditional adversarial networks,” in *CVPR*, 2017.
- [28] Jun-Yan Zhu et al., “Toward multimodal image-to-image translation,” in *NeurIPS*, 2017.
- [29] Nelson Nauata, Kai-Hung Chang, Chin-Yi Cheng, Greg Mori, and Yasutaka Furukawa, “House-gan: Relational generative adversarial networks for graph-constrained house layout generation,” in *ECCV*, 2020.
- [30] Yunjey Choi et al., “Stargan: Unified generative adversarial networks for multi-domain image-to-image translation,” in *CVPR*, 2018.
- [31] Xun Huang, Ming-Yu Liu, et al., “Multimodal unsupervised image-to-image translation,” in *ECCV*, 2018.
- [32] Taesung Park et al., “Contrastive learning for unpaired image-to-image translation,” in *ECCV*, 2020.
- [33] Chitwan Saharia et al., “Image super-resolution via iterative refinement,” *IEEE PAMI*, 2022.
- [34] Chitwan Saharia, William Chan, Huiwen Chang, Chris Lee, Jonathan Ho, Tim Salimans, David Fleet, and Mohammad Norouzi, “Palette: Image-to-image diffusion models,” in *ACM SIGGRAPH 2022 Conference Proceedings*, 2022, pp. 1–10.
- [35] Robin Rombach, Andreas Blattmann, Dominik Lorenz, Patrick Esser, and Björn Ommer, “High-resolution image synthesis with latent diffusion models,” in *Proceedings of the IEEE/CVF Conference on Computer Vision and Pattern Recognition*, 2022, pp. 10684–10695.
- [36] Wanyi Li et al., “Unsupervised image-generation enhanced adaptation for object detection in thermal images,” *arXiv*, 2020.
- [37] Guan-An Wang et al., “Cross-modality paired-images generation for rgb-infrared person re-identification,” in *AAAI*, 2020.
- [38] Tianren Wang, Teng Zhang, Liangchen Liu, Arnold Willem, and Brian Lovell, “Cannygan: Edge-preserving image translation with disentangled,” .
- [39] Qifeng Chen and Vladlen Koltun, “Photographic image synthesis with cascaded refinement networks,” in *Proceedings of the IEEE international conference on computer vision*, 2017, pp. 1511–1520.
- [40] Khawla Mallat and Jean-Luc Dugelay, “Indirect synthetic attack on thermal face biometric systems via visible-to-thermal spectrum conversion,” in *CVPR*, 2021.
- [41] Min Jin Chong et al., “Gans n’roses: Stable, controllable, diverse image to image translation (works for videos too!),” *arXiv*, 2021.
- [42] Vicente Pavez, Gabriel Hermosilla, Francisco Pizarro, Sebastián Fingerhuth, and Daniel Yunge, “Thermal image generation for robust face recognition,” *Applied Sciences*, 2022.
- [43] Olaf Ronneberger et al., “U-net: Convolutional networks for biomedical image segmentation,” in *MICCAI*, 2015.
- [44] Virginia Espinosa-Duró, Marcos Faundez-Zanuy, and Jiří Mekyska, “A new face database simultaneously acquired in visible, near-infrared and thermal spectrums,” *Cognitive Computation*, 2013.
- [45] Dario Fuoli et al., “Fourier space losses for efficient perceptual image super-resolution,” in *CVPR*, 2021, pp. 2360–2369.
- [46] Richard Zhang, “Making convolutional networks shift-invariant again,” in *ICML*, 2019.
- [47] Mostafa Sharifzadeh, Habib Benali, and Hassan Rivaz, “Investigating shift variance of convolutional neural networks in ultrasound image segmentation,” *IEEE Transactions on Ultrasonics, Ferroelectrics, and Frequency Control*, vol. 69, no. 5, pp. 1703–1713, 2022.
- [48] Takeru Miyato et al., “Spectral normalization for generative adversarial networks,” *arXiv*, 2018.
- [49] Kilian Q Weinberger and Lawrence K Saul, “Distance metric learning for large margin nearest neighbor classification.,” *JMLR*, vol. 10, no. 2, 2009.
- [50] “Your perfect palette flir - understanding thermal palettes,” .
- [51] Manuel Fritsche, Shuhang Gu, and Radu Timofte, “Frequency separation for real-world super-resolution,” in *2019 IEEE/CVF International Conference on Computer Vision Workshop (ICCVW)*. IEEE, 2019.
- [52] Younghyun Jo, Sejong Yang, and Seon Joo Kim, “Investigating loss functions for extreme super-resolution,” in *CVPR Workshops*, 2020.
- [53] Royson Lee, Łukasz Dudziak, Mohamed Abdelfattah, Stylianos I Venieris, Hyeji Kim, Hongkai Wen, and Nicholas D Lane, “Journey towards tiny perceptual super-resolution,” in *ECCV*, 2020.
- [54] Karen Simonyan and Andrew Zisserman, “Very deep convolutional networks for large-scale image recognition,” *arXiv*, 2014.

- [55] Alexia Jolicoeur-Martineau, “The relativistic discriminator: a key element missing from standard gan,” *arXiv*, 2018.
- [56] Xintao Wang, Ke Yu, Shixiang Wu, Jinjin Gu, Yihao Liu, Chao Dong, Yu Qiao, and Chen Change Loy, “Esrgan: Enhanced super-resolution generative adversarial networks,” in *ECCV*, 2018.
- [57] Khawla Mallat et al., “A benchmark database of visible and thermal paired face images across multiple variations,” in *BIOSIG*, 2018.
- [58] Domenick Poster, Matthew Thielke, et al., “A large-scale, time-synchronized visible and thermal face dataset,” in *WACV*, 2021.
- [59] Domenick D Poster, Shuowen Hu, Nathan J Short, Benjamin S Riggan, and Nasser M Nasrabadi, “Visible-to-thermal transfer learning for facial landmark detection,” *IEEE Access*, 2021.
- [60] Chichen Fu, Soonam Lee, David Joon Ho, Shuo Han, Paul Salama, Kenneth W Dunn, and Edward J Delp, “Three dimensional fluorescence microscopy image synthesis and segmentation,” in *Proceedings of the IEEE conference on computer vision and pattern recognition workshops*, 2018, pp. 2221–2229.
- [61] Nima Tajbakhsh, Laura Jeyaseelan, Qian Li, Jeffrey N Chiang, Zhihao Wu, and Xiaowei Ding, “Embracing imperfect datasets: A review of deep learning solutions for medical image segmentation,” *Medical Image Analysis*, vol. 63, pp. 101693, 2020.
- [62] Zhenlin Xu and Marc Niethammer, “Deepatlas: Joint semi-supervised learning of image registration and segmentation,” in *International Conference on Medical Image Computing and Computer-Assisted Intervention*. Springer, 2019, pp. 420–429.
- [63] Taesung Park et al., “Semantic image synthesis with spatially-adaptive normalization,” in *CVPR*, 2019, pp. 2337–2346.
- [64] Martin Heusel et al., “Gans trained by a two time-scale update rule converge to a local nash equilibrium,” *NeurIPS*, 2017.
- [65] Weixia Zhang et al., “Blind image quality assessment using a deep bilinear convolutional neural network,” *IEEE CSVT*, vol. 30, no. 1, pp. 36–47, 2018.
- [66] Alain Hore and Djemel Ziou, “Image quality metrics: Psnr vs. ssim,” in *ICPR*, 2010.
- [67] Jim Nilsson and Tomas Akenine-Möller, “Understanding ssim,” *arXiv preprint arXiv:2006.13846*, 2020.
- [68] Lili Lin, Hong Chen, Ercan Engin Kuruoglu, and Wenhui Zhou, “Robust structural similarity index measure for images with non-gaussian distortions,” *Pattern Recognition Letters*, vol. 163, pp. 10–16, 2022.
- [69] Sidi Yang, Tianhe Wu, Shuwei Shi, Shanshan Lao, Yuan Gong, Mingdeng Cao, Jiahao Wang, and Yujiu Yang, “Maniqa: Multi-dimension attention network for no-reference image quality assessment,” in *Proceedings of the IEEE/CVF Conference on Computer Vision and Pattern Recognition*, 2022, pp. 1191–1200.
- [70] Jean-François Pambrun and Rita Noumeir, “Limitations of the ssim quality metric in the context of diagnostic imaging,” in *International Conference on Image Processing*, 2015.
- [71] Irving A Cruz-Albarran, Juan P Benitez-Rangel, Roque A Osornio-Rios, and Luis A Morales-Hernandez, “Human emotions detection based on a smart-thermal system of thermographic images,” *Infrared Physics & Technology*, vol. 81, pp. 250–261, 2017.
- [72] Xun Huang, Ming-Yu Liu, Serge Belongie, and Jan Kautz, “Multimodal unsupervised image-to-image translation,” in *ECCV*, 2018.
- [73] Francesco Pittaluga, Aleksandar Zivkovic, and Sanjeev J Koppal, “Sensor-level privacy for thermal cameras,” in *2016 IEEE International Conference on Computational Photography (ICCP)*. IEEE, 2016, pp. 1–12.